



# Design and measurement of a multi-feed resonant cavity antenna with in-antenna power combination at mm-wave

Khushboo Singh<sup>1</sup> , Ronald Mulinde<sup>2</sup>, Manik Attygalle<sup>2</sup>,  
Dushmantha N. Thalakituna<sup>1</sup>, Karu P. Esselle<sup>1</sup> and Abu Sadat Md. Sayem<sup>3</sup>

<sup>1</sup>School of Electrical and Data Engineering, University of Technology Sydney, Sydney, NSW, Australia; <sup>2</sup>DSTG, Edinburgh, Australia and <sup>3</sup>School of Engineering, Macquarie University, Sydney, NSW, Australia

## Research Paper

**Cite this article:** Singh K, Mulinde R, Attygalle M, Thalakituna DN, Esselle KP, Sayem ASM (2025) Design and measurement of a multi-feed resonant cavity antenna with in-antenna power combination at mm-wave. *International Journal of Microwave and Wireless Technologies*, 1–12. <https://doi.org/10.1017/S1759078725000479>

Received: 30 September 2024  
Revised: 23 March 2025  
Accepted: 27 March 2025

### Keywords:

High-power antenna; multi-feed; dielectric resonators; resonant cavity antenna; in-antenna power combination; mm-wave; partially reflecting superstrate; high-gain

**Corresponding author:** Khushboo Singh;  
Email: [khushboo.singh@uts.edu.au](mailto:khushboo.singh@uts.edu.au)

### Abstract

In this paper, we present the design, simulation, fabrication, and measurements of an on-chip dielectric resonator (DR)-fed millimeter-wave high-gain antenna system with in-antenna power combining capability. A low-profile resonant cavity antenna is fed by four spherical DR, showcasing the antenna's multi-feed capabilities. Each DR is fed by two microstrip resonators located diagonally opposite on a planar circuit board and are excited via coaxial connectors. The design incorporates a printed partially reflecting superstrate, reducing the antenna's overall size and profile while simultaneously enhancing directivity by approximately 10 dB at the design frequency of 30 GHz. The antenna exhibits wideband matching. Key performance metrics, such as directivity, gain, beamwidth, and bandwidth, predicted by full-wave electromagnetic simulations align well with the results from experimental measurements.

### Introduction

The demand for higher data rates is greater than ever, driven by the proliferation of cloud and online-based applications that require uninterrupted, low-latency, and high-speed data. 5G technology is well suited to meet these needs. Millimeter-wave (mm-wave) wireless communication has become a standard for 5G and beyond due to its capability to deliver high data throughput, low latency, and reduced energy consumption, effectively supporting the growing number of users and smart devices [1]. With its high carrier frequency, mm-wave can transmit more data per baud, leading to higher data rates (bits per second per Hz) and reduced buffering times for high-quality video streaming. Additionally, mm-wave technology is employed in radar and image sensing, next-generation Wi-Fi (WiGig), virtual reality for 3D rendering, as well as medical, military, and Internet of things applications [2].

Despite its numerous benefits, mm-wave communication suffers from significant atmospheric losses, which limit its coverage range. However, this limitation can be advantageous for cellular communication, as it allows for network coverage expansion through techniques like frequency reuse, cell splitting, and sectoring. To unlock the advantages of mm-wave communication, it is essential to deploy structurally simple, highly efficient high-power antenna (transmit/receive) subsystems. These subsystems must effectively compensate for the substantial free-space path loss at mm-wave frequencies, which increases proportionally to the square of the frequency [3]. Various antenna solutions utilizing power-combining techniques have been proposed to date. These solutions include spatial multiplexing within large antenna arrays, and multi-feed antennas with on-air power combining capabilities to boost the effective isotropic radiated power and counteract losses [4]. However, each of these antenna technologies faces distinct limitations, such as challenges with packaging, thermal management, substantial on-chip space requirements, the need for unconventional signal processing techniques, restricted radiation efficiency, bandwidth constraints, and complex design architectures [5].

Self-aligning on-chip dielectric resonators (DRs) are engineered to optimize radiation efficiency at mm-wave frequencies, ensuring that a substantial portion of the input power is effectively radiated from the chip. In the past, self-aligning spherical DRs have been utilized alongside dielectric superstrates, artificial surfaces, and resonant cavity antennas (RCAs) to enhance overall radiation properties [6]. In this research, we investigate the performance of an on-chip DR-fed RCA antenna [4] using full-wave electromagnetic (EM) simulations. This is followed by the fabrication and measurement of a prototype. Our design features a low-profile, low-loss, high-gain RCA with multiple inputs, operating in the mm-wave spectrum and incorporating in-antenna power-combining capabilities. The RCA is excited by four low-loss spherical DRs, demonstrating its capability to support multiple feeds. Each DR is fed by

© The Author(s), 2025. Published by Cambridge University Press in association with The European Microwave Association. This is an Open Access article, distributed under the terms of the Creative Commons Attribution licence (<http://creativecommons.org/licenses/by/4.0>), which permits unrestricted re-use, distribution and reproduction, provided the original article is properly cited.

two microstrip resonators positioned diagonally opposite each other on a planar printed circuit board (PCB), with signals of equal amplitude and a phase difference of  $180^\circ$ . The microstrip resonators are vertically probe-fed using sub-miniature push-on micro (SMPM)-type connectors. This choice helps effectively mitigate losses in the feed transmission lines. The spatial separation of these feed resonators can be adjusted as required. Additionally, a printed partially reflecting superstrate (PRS) is used instead of the uniform PRS typically employed in traditional RCAs to both enhance the overall directivity and minimize both the antenna's size and profile.

An earlier version of this paper was presented at the 18th edition of the European Conference on Antennas and Propagation (EuCAP) and was published in its proceedings [7]. It covered the theoretical aspects and design methodology of the antenna discussed in this work. This article details the fabrication and assembly of the multi-input RCA, alongside an experimental analysis that provides insights into its performance. A performance evaluation of key parameters – such as active reflection coefficients, gain, and radiation patterns – was conducted at five frequencies within the desired bandwidth. The results align with theoretical predictions and simulations. New graphics added to this article enhance the understanding of the feeding mechanism and the system as a whole.

The rest of the article is organized as follows: Design methodology section describes the design methodology for the proposed mm-wave antenna. Simulation results section presents simulation results for the multi-feed RCA design. Antenna fabrication, measurement and experimental results section details the antenna fabrication and assembly challenges and discusses the experiments conducted to validate and verify the performance of the RCA. The measured results are shown and analyzed against simulations in Analysis and Discussion of Results section. Finally, Conclusion section provides the concluding remarks and some insights into potential future work.

## Design methodology

Figure 1 illustrates the complete schematic of the on-chip spherical DR-fed RCA with eight input ports. The antenna is constructed from three distinct layers of PCB: the bottom layer made of Rogers RT6202 ( $\epsilon_r = 2.94$  and  $\tan \delta = 0.0015$ ), 0.508 mm thick middle board of Rogers RT5880 ( $\epsilon_r = 2.2$  and  $\tan \delta = 0.0009$ ), and the top printed superstrate layer of Rogers TMM4 ( $\epsilon_r = 4.5$  and  $\tan \delta = 0.002$ ). Four circular crates are precisely machined into the top of the chip layer to accommodate the four DRs. The middle board is then positioned on top, featuring square metallic patches with circular slots. These slots are aligned directly above the crates, ensuring that the dielectric spheres fit securely between the crates in the chip layer and the slots in the middle board. Screws and spacers are installed at each of the four corners of the antenna. The screws pass through the holes in the spacers and are tightened to press the dielectric spheres firmly against the chip. This setup ensures that the DRs remain firmly in place and do not dislocate during installation or operation. By doing so, the non-radiant modes of the DRs are excited, with the  $TE_{112}$  mode providing the strongest coupling to the chip [8]. The resonance frequency of the DRs is determined using Equation (1):

$$f_{\text{res}} \text{ (GHz)} = \frac{a}{d \text{ (mm)}}, \quad (1)$$

where  $d$  is the diameter of the spherical DR. The constant  $a$  is specific to the modes and is determined by the effective dielectric constant of the DR.

For this design, the DR is made of alumina ( $Al_2O_3$ ), which has a dielectric constant of 9.8 and a low loss tangent of less than 0.001 up to a frequency of 100 GHz. The parameter  $a$  is 104.3 for the  $TE_{112}$  mode [9]. At the operating frequency of 30 GHz, the diameter of the DR is approximately 3.5 mm, considering that the middle board on top of the spheres excites the  $TE_{112}$  mode. To enable power combination within the antenna, the non-radiating  $TE_{112}$  mode which exhibits electric symmetry is excited from two different directions by two diagonally opposite microstrip resonators each measuring  $\frac{\lambda_g}{4}$  in length, where  $\lambda_g$  is the guided wavelength. These resonators are probe-fed with equal amplitudes and a phase difference of  $180^\circ$  using SMPM-type RF coaxial connectors [10]. Four circular coupling slots on the lower ground layer of the middle board located above each spherical DR facilitate the coupling of the non-radiating modes of each DR to the microstrip patch radiator on the top layer of the middle board.

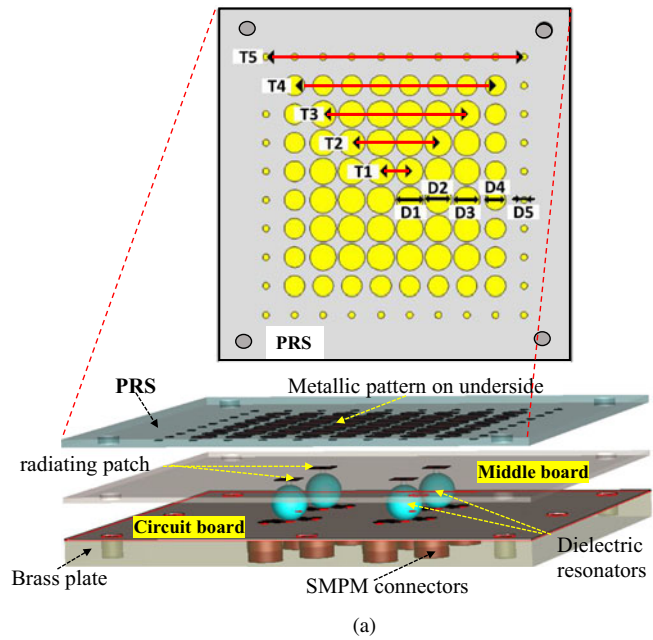
A printed PRS board is positioned at height  $L_r$  above the middle board, forming a resonant cavity. This configuration allows the EM fields to undergo multiple reflections, which leads to resonance and enhances the antenna's directivity and overall radiation performance. The value of  $L_r$  is calculated from [11] according to Equation (2):

$$\frac{4\pi L_r}{\lambda_0} = 2N\pi - \phi_{\text{ground}} - \phi_{\text{PRS}}, \quad (2)$$

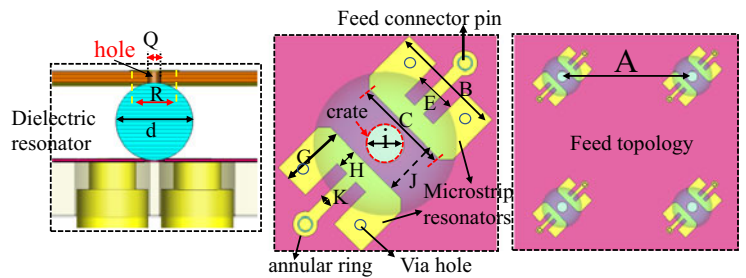
where  $\lambda_0$  represents the free space wavelength at the operating frequency,  $N$  is the vertical wave number,  $\phi_{\text{ground}}$  and  $\phi_{\text{PRS}}$  are the phase delays introduced in the electric field after reflection from the ground and the PRS, respectively. We assume that  $\phi_{\text{ground}} = \phi_{\text{PRS}} = -\pi$ . Hence, the smallest cavity length for fundamental resonance is  $L_r = \frac{\lambda_0}{2}$  [12].

Figure 1(a) displays an isometric view of the antenna model, including an expanded back view of the thin printed PRS. Alongside creating a resonant cavity in the antenna, the printed PRS also creates a more uniform aperture phase distribution above the patch radiators. The PRS is composed of Rogers TMM4 with circular metallic patches printed on the underside facing the patch radiators. The diameters of the circular metallic patches ( $D1$ ,  $D2$ ,  $D3$ ,  $D4$ , and  $D5$ ) printed on the bottom side of the PRS decrease gradually from the center toward the edge. This configuration adds more phase delay to the field at the center compared to the edges. The PRS plays a crucial role in determining the antenna's radiation properties, including directivity and radiation pattern. For more detailed information on the design of printed PRS, readers are referred to [12].

Figure 2 illustrates the feeding arrangement used to excite the DRs, which are mounted on top of the circuit board shown in Figure 1(a). Each of the DRs (in bronze) is fed by two microstrip resonators (in red and black) located diagonally opposite. These microstrip resonators are probe-fed with equal amplitudes and a phase difference of  $180^\circ$  using SMPM-type RF coaxial connectors [10]. This arrangement excites the same non-radiating modes from two different directions, achieving constructive power combining. Additionally, four coupling slots are incorporated into the lower ground layer of the middle board to facilitate the coupling of the non-radiating modes of each DR to the microstrip patch radiator positioned on the top layer directly above each spherical DR.



(a)



(b)

**Figure 1.** Design configuration of the on-chip multi-feed resonant cavity antenna system. (a) Isometric view of the antenna simulation model showing an expanded back view of the PRS [7] and (b) expanded view of a DR, coupling slot, and alignment hole, DR fed by two microstrip resonators and the feed topology of the complete antenna [7].

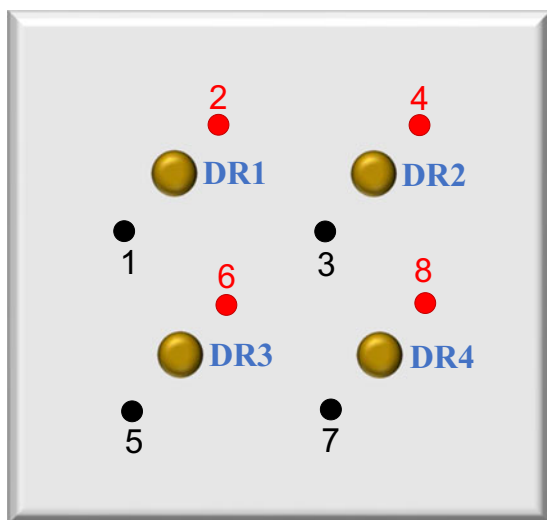


**Figure 2.** Bottom view of the antenna showing the microstrip resonator feed pairs (black) and (red) and DRs (bronze). Feed pairs (1, 2), (3, 4), (5, 6), and (7, 8) feed DRs-1, 2, 3, and 4, respectively [13].

**Simulation results**

The proposed eight-input RCA was modeled in CST MWS, and full-wave EM simulations were conducted using the time domain solver. Figure 3 shows the simulated return loss for

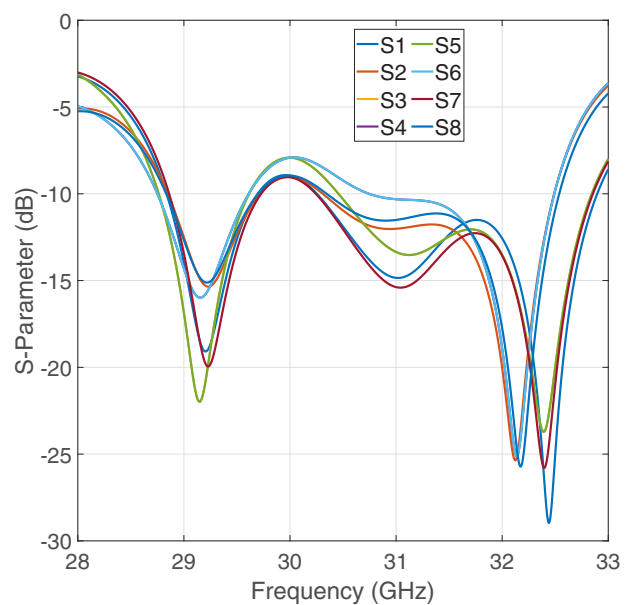


**Figure 3.** Simulated return loss at each input port of the antenna [7].

each input port (when all ports are excited simultaneously). The antenna demonstrates excellent matching, with a return loss of less than  $-8$  dB across all eight input ports within the frequency

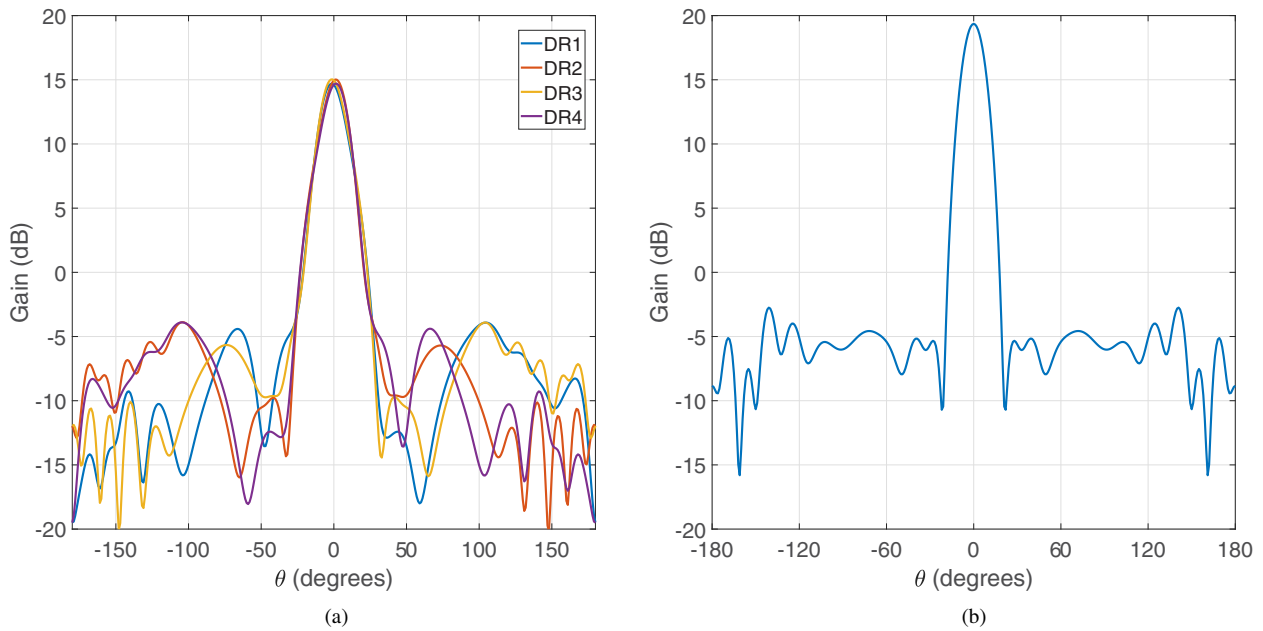


**Figure 4.** Simulated realized gain pattern for the 8-port RCA at 30 GHz [13]. (a) Individual DRs. (b) Antenna system.

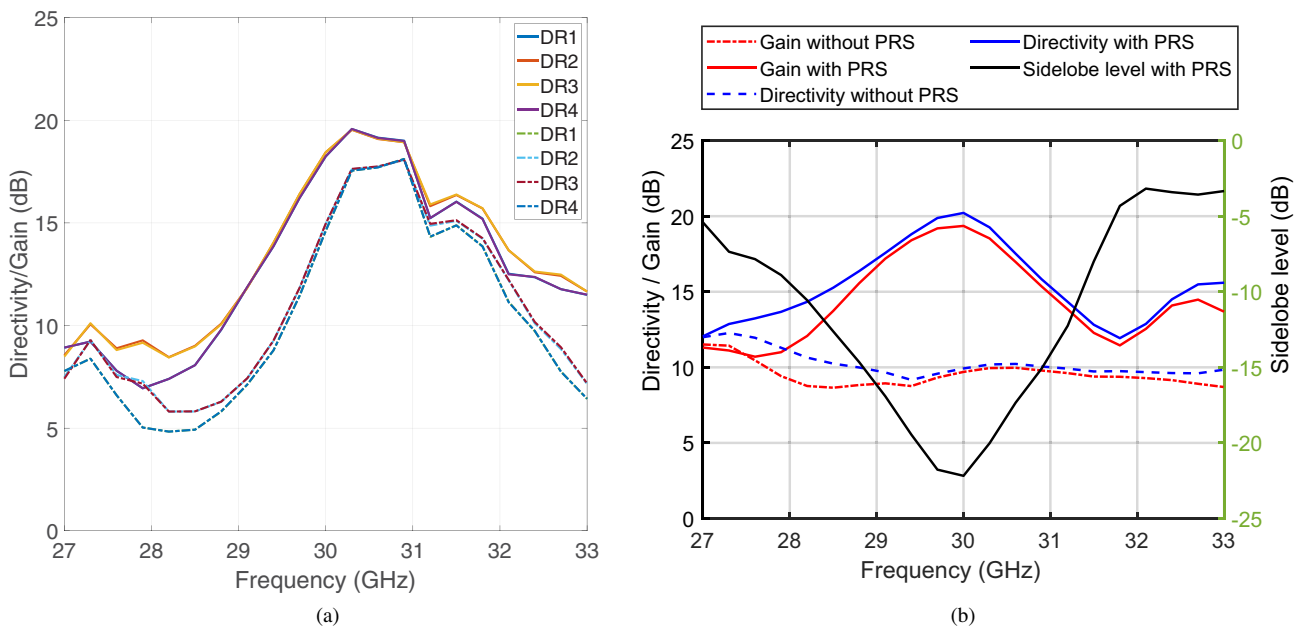


**Figure 5.** Simulated radiation characteristics for the 8-port RCA at boresight, with directivity (solid) and gain (dashed). (a) Individual DRs. (b) Gain, directivity, and sidelobe level over frequency for the antenna system.

range of 28.8–32.5 GHz. The weak coupling of the feeding elements arises from signal leakage from the edges to the top, which enables the integration of multiple feeding DRs within the same chip area without impacting the input impedance of the feeds. An outstanding in-antenna power combination is achieved by exciting the same non-radiating resonance modes in each feeding DR. Figure 4 shows the simulated radiation pattern for each individual DR (see Figure 4(a)) as well as the radiation pattern for the overall antenna system at 30 GHz (see Figure 4(b)).

Figure 5(a) illustrates the variations in the simulated directivity and realized antenna gain over frequency when each DR is

excited individually. The variations in gain and directivity are consistent with the reciprocal behavior of the antenna. Specifically, odd-numbered, DR1 and DR3 exhibit similar and closely matching responses, while even-numbered, DR2 and DR4 also display similar and closely matching responses. Figure 5(b) shows the simulated directivity and realized gain variation of the antenna system over the same frequency range, with and without the printed PRS. It can be observed that the PRS increases the overall directivity and realized gain of the antenna. A peak gain enhancement of approximately 10 dB is achieved at the design frequency of 30 GHz. A maximum simulated directivity of 20.1 dB and a maximum

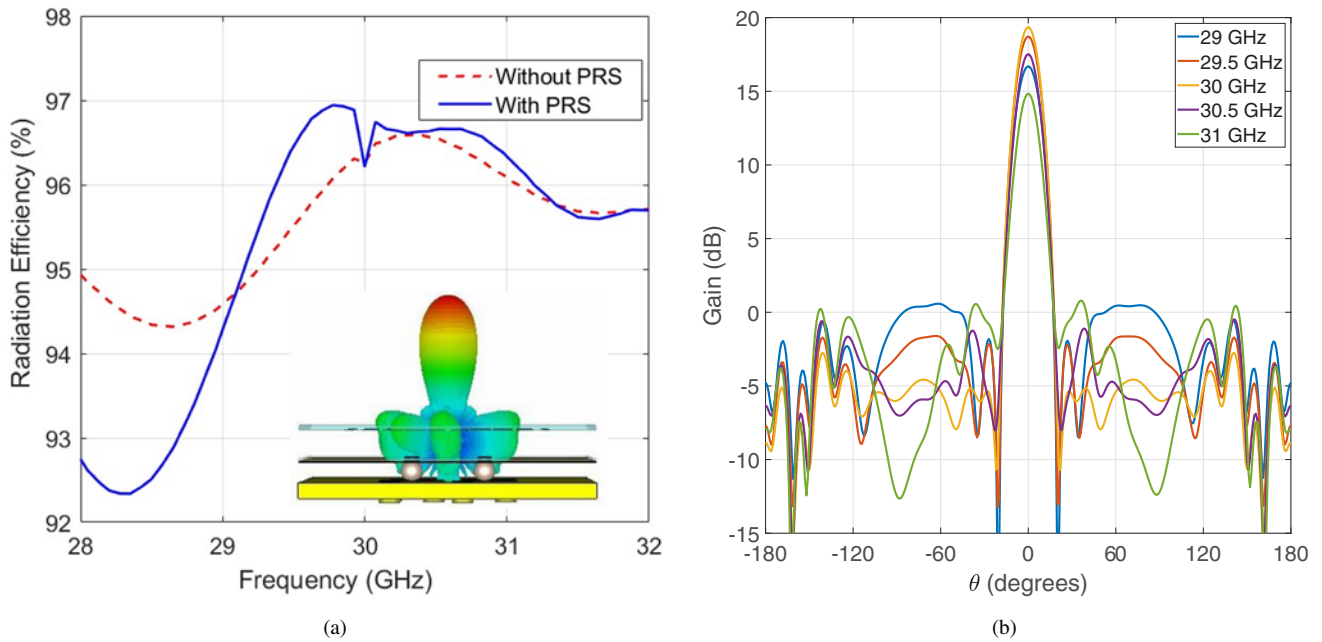


**Figure 6.** Characteristics of the multi-feed RCA. (a) Radiation efficiency plots with and without the PRS [7] featuring a 3D radiation pattern at 30 GHz shown as an inset. (b) Elevation radiation pattern cut for different frequencies at  $\phi = 0^\circ$ .

realized gain of 19.4 dB at 30 GHz are achieved. The 3 dB gain bandwidth of the antenna is approximately 1.9 GHz from 28.9 GHz to 30.8 GHz. Figure 5(b) also shows the maximum sidelobe levels against frequency. The sidelobes are consistently below  $-10$  dB across the frequency range of 28.18–31.45 GHz.

Figure 6(a) compares the radiation efficiency between the proposed antennas with and without the PRS. The radiation efficiency of the antenna featuring the PRS remains largely comparable to that of the antenna without it, showing only a slight decrease of about 2% within the frequency range of 28–29 GHz. It was observed that the radiation efficiency exceeds 93.3% and the total efficiency remains above 81.6% across the frequency range of 28.8–32.6 GHz. A 3D radiation pattern obtained at 30 GHz is presented as an inset in Figure 6(a).

To demonstrate the radiation pattern characteristics of the designed antenna, the elevation-plane radiation pattern for the antenna is illustrated for five different frequencies within the operating band in Figure 6(b). The maximum realized gain occurs at the design frequency of 30 GHz.

### Antenna fabrication, measurement, and experimental results

Following the design description in Design methodology section, a prototype of the on-chip DR-fed RCA with eight inputs was fabricated and measured. The design parameters are provided in Table 1, and a comparison between the measured and simulated return loss at each port is shown in Figure 7. The thickness of the conductor on the middle board is 0.035 mm and is 0.017 mm on the PRS and the circuit board. The side length of all the square boards and the brass plate is  $O = 45$  mm. A strategic approach has been adopted to assemble the antenna, ensuring that the DRs are secured tightly. The three separately fabricated boards (circuit board, middle board, and the PRS) are assembled with the spherical DRs and

**Table 1.** Design parameter values for the proposed antenna [7]

Design parameters	mm	Design parameters	mm
O	45	RT <sub>5880</sub>	0.508
M	3.386	Th <sub>ultra</sub>	0.127
A	12.99	Th <sub>TMM</sub>	0.76
P	1.887	D1	3.2004
L <sub>r</sub>	4.7	D2	3.1956
R	2.076	D3	3.144
G	1.4187	D4	2.448
B	2.445	D5	0.816
H	0.425	T1	3.402
E	1.132	T2	10.2072
G	1.4187	T3	17.0112
B	2.445	T4	23.8164
H	0.425	T5	30.6204
E	1.132	E	1.132
K	0.255	H	0.425
G	1.4187	B	2.445
Q	0.58	d	3.5

a supporting brass plate using nylon spacers and polyvinylidene fluoride plastic screws. Through holes were drilled on the boards and brass plate to provide passage for screws during assembly and packaging. The three boards are aligned accurately by inserting plastic screws, and proper spacing between the layers is maintained using 3D-printed nylon spacers. The nylon spacers have through

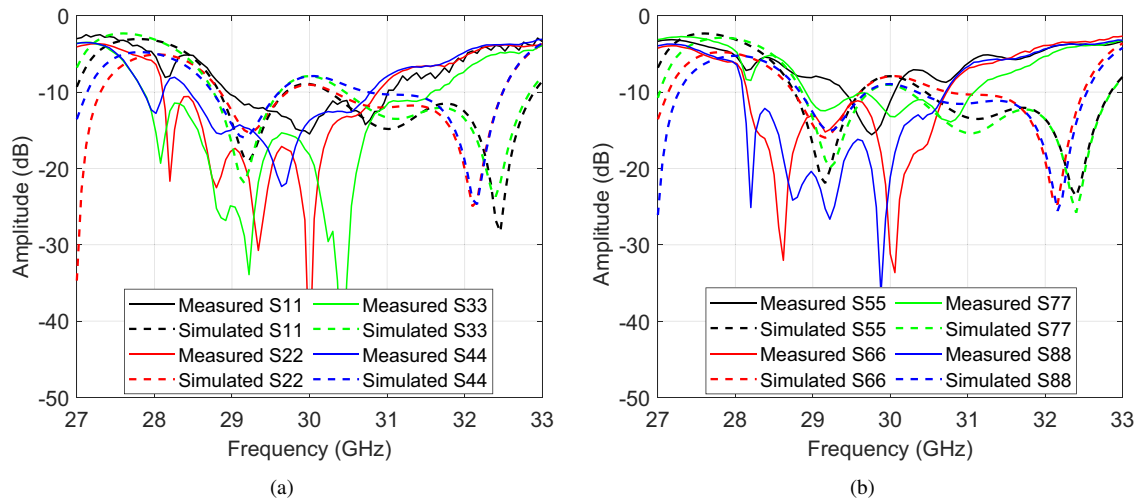


**Figure 7.** Measured and simulated return loss at (a) port 1 to port 4 (S11, S22, S33, S44) and (b) port 5 to port 8 (S55, S66, S77, and S88).

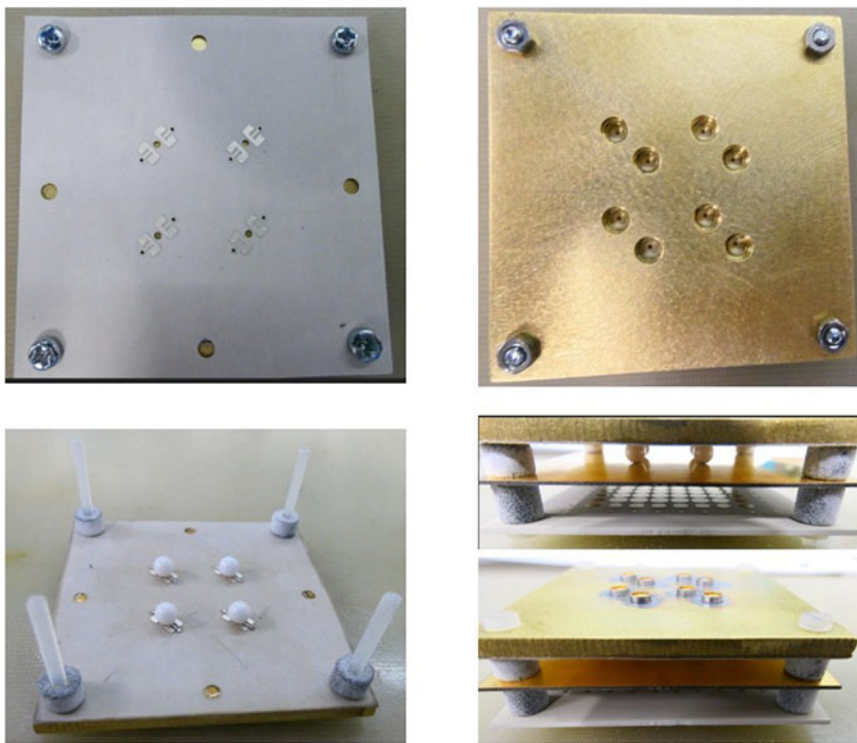


**Figure 8.** Fabricated components: circuit board (top left), brass plate (top right), DRs positioned on the crate within the circuit board and 3D-printed nylon spacers (bottom left), assembly and packaging of the RCA.

holes to allow the screws to pass. A 2.5 mm thick brass plate is positioned beneath the circuit board to enhance the design's sturdiness and durability, especially given the circuit board's thickness of just 0.508 mm. This added support helps to prevent flexing and ensures structural integrity, thereby contributing to the overall reliability of the assembly. The brass plate further acts as a cover for the alignment holes on the substrate, preventing radiation leakage. The assembly process is pictorially illustrated in Figure 8. First, plastic screws are inserted into the four corner holes of the brass plate, providing a secure foundation.

The bottom circuit board is then placed directly on top of the brass support layer, with the four corner holes aligned over the

screw legs at each corner, allowing it to slide into position. To maintain an appropriate gap between the middle layer and the circuit board, four nylon spacers with center-through holes are added, one at each screw location, by sliding them over the screw legs. Next, four spherical DRs are positioned on the four crates within the circuit board. The middle board is then placed, allowing its corners to slide over the same screw legs at each corner. Another set of four nylon spacers is added, one at each corner, by sliding them over the screw legs. These spacers create the necessary height to form a resonant cavity. Finally, the PRS is added, with its four corner holes aligned with the same four screw legs at each corner. Bolts are used to fasten the screws, ensuring that the assembly is secure

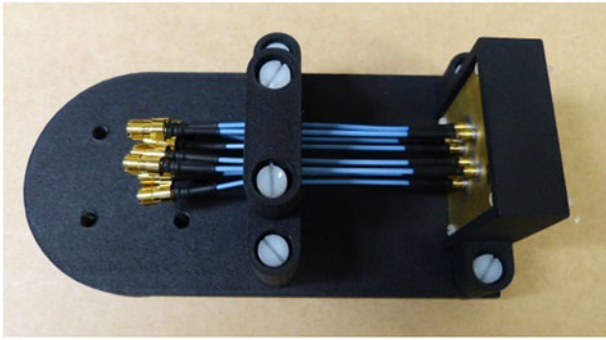


**Figure 9.** Assembled RCA with a 3D-printed mount.

and prevents displacement of the spheres after packaging. This careful assembly process enhances both stability and performance in the final design.

While Figure 8 displays the fabricated components and the assembled antenna prototype, Figure 9 shows the RCA installed in a 3D-printed antenna mount, and the high-frequency RF cables that were connected to each input port. S-parameters were measured using a multi-port vector network analyzer (VNA) (Figure 7). The measured return loss at all ports, except for port-1 (S11), is below  $-8$  dB between 27.8 GHz and 30.7 GHz. For port 1, the return loss goes up to  $-6$  dB between 27.6 GHz and 28.8 GHz but remains below  $-8$  dB from 28.8 GHz to 30.2 GHz. The variation in port-1 matching could be due to lossy cables. To ensure consistent measurement of the multi-input antenna, we validate the results using the following three different measurement setups.

- Measurement setup I: a 2-port VNA is used for obtaining the gain for each DR. The transmit path to each DR is identical.
- Measurement setup II: a 2-port VNA is used for obtaining the gain for each DR. However, different transmit paths are used while testing each DR.
- Measurement setup III: a multichannel arbitrary waveform generator (AWG) is used to simultaneously excite all DRs via different transmit paths.

### Individual DR excitation

We investigate the performance of the antenna with individual DR excitation using measurement setups I and II.

### Measurement setup I

A schematic for the transmit chain used for performing measurements with independent individual excitations is shown in Figure 10.

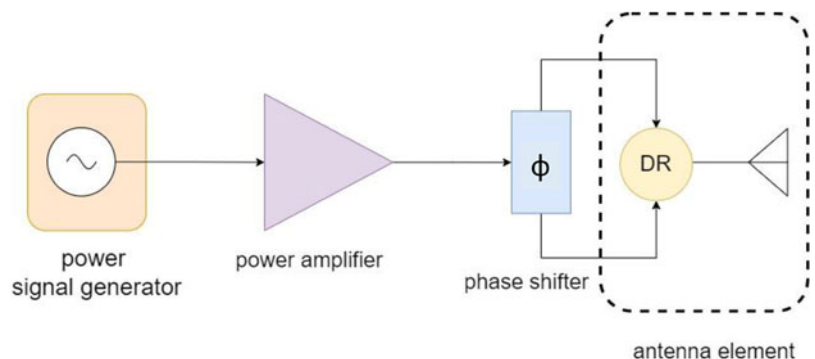
A 2-port VNA was used to characterize the transmission path from the signal generator to the receiver. This same transmission path is used for studying the behavior of each DR. In this transmit chain (Figure 12(a)), a single channel signal generator feeds a power amplifier (PA). The output of the PA feeds the input port of a phase shifter. The pair of outputs from the phase shifter, with a phase difference of  $180^\circ$  in turn, excite each individual DR of the RCA. While each DR was excited, the other six input ports of the RCA that feed the rest of the DRs were terminated using 50 dB matched loads. A single channel signal generator, therefore, excites each spherical DR (see Figure 10). In measurement setup I, for characterizing each individual DR, the output power from the single channel signal generator was set to 0 dBm. A standard gain horn (SGH) antenna was used to collect the signal at the receiver side. The antenna gain corresponding to each DR was measured and is shown in Figure 11(a) and (b). Figure 11(a) plots the elevation plane radiation pattern cut for each DR at a center frequency of 30 GHz as measured in an anechoic chamber. The main lobes for DR1, DR2, DR3, and DR4 exhibit peaks at 9.74 dB, 9.49 dB, 10.58 dB, and 10.09 dB, respectively with corresponding offsets from boresight at  $-3^\circ$ ,  $9^\circ$ ,  $0^\circ$ , and  $10.0^\circ$ , respectively.

Figure 11(b) shows the measured peak gain against frequency for each DR in the 28–32 GHz frequency range. The peak gains for DR1, DR2, DR3, and DR4 are 10.59 dB, 10.06 dB, 10.76 dB, and 10.09 dB at frequencies of 30.5 GHz, 30.5 GHz, 30.5 GHz, and 30 GHz, respectively. In this frequency range, DR3 exhibits the highest peak gain of 10.76 at 30.5 GHz, while DR2 exhibits the lowest peak gain of 10.06 at 30.5 GHz.

### Measurement setup II

The setup for the transmit chain illustrated in Figure 12(a) was used to investigate the performance of each DR with independent transmit paths. The results from these measurements are presented in Figure 13. Figure 13(a) plots the elevation plane radiation pattern cut for each DR of the RCA at a center frequency of 30 GHz. The main lobes for DR1, DR2, DR3, and DR4 exhibit peaks at 10.16 dB, 10.45 dB, 10.56 dB, and 10.67 dB, respectively, with corresponding offsets from boresight at  $-1.5^\circ$ ,  $8^\circ$ ,  $1^\circ$ , and  $9^\circ$ , respectively.

Figure 13(b) shows the measured peak gain against frequency for each DR in the 28–32 GHz frequency range. The peak gains for DR1, DR2, DR3, and DR4 are 11.36 dB, 10.97 dB, 11.56 dB, and 10.78 dB at frequencies of 30.5 GHz, 30.5 GHz, 30 GHz, and 10.78 dB at frequencies of 30.5 GHz, 30.5 GHz, 30 GHz,



**Figure 10.** Transmit chain setup for individual DR – measurement setup I.

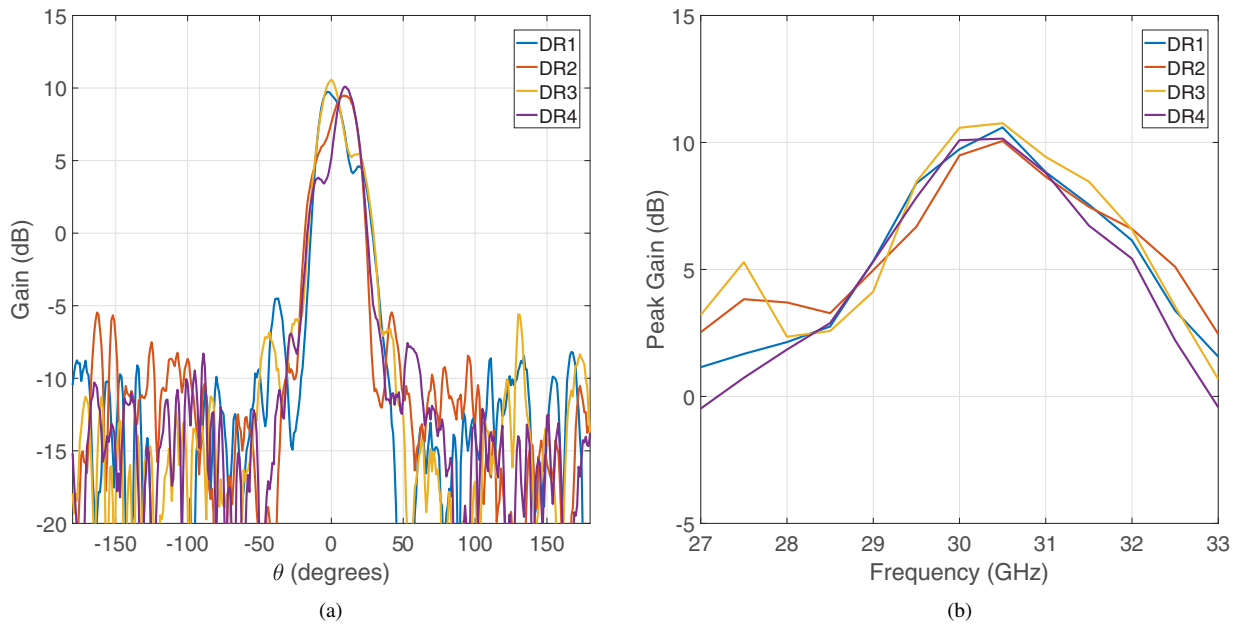


**Figure 11.** Measured radiation performance of the RCA with individual DR excitation with measurement setup I. (a) Elevation plane radiation pattern cut at 30 GHz. (b) Peak gain vs frequency.

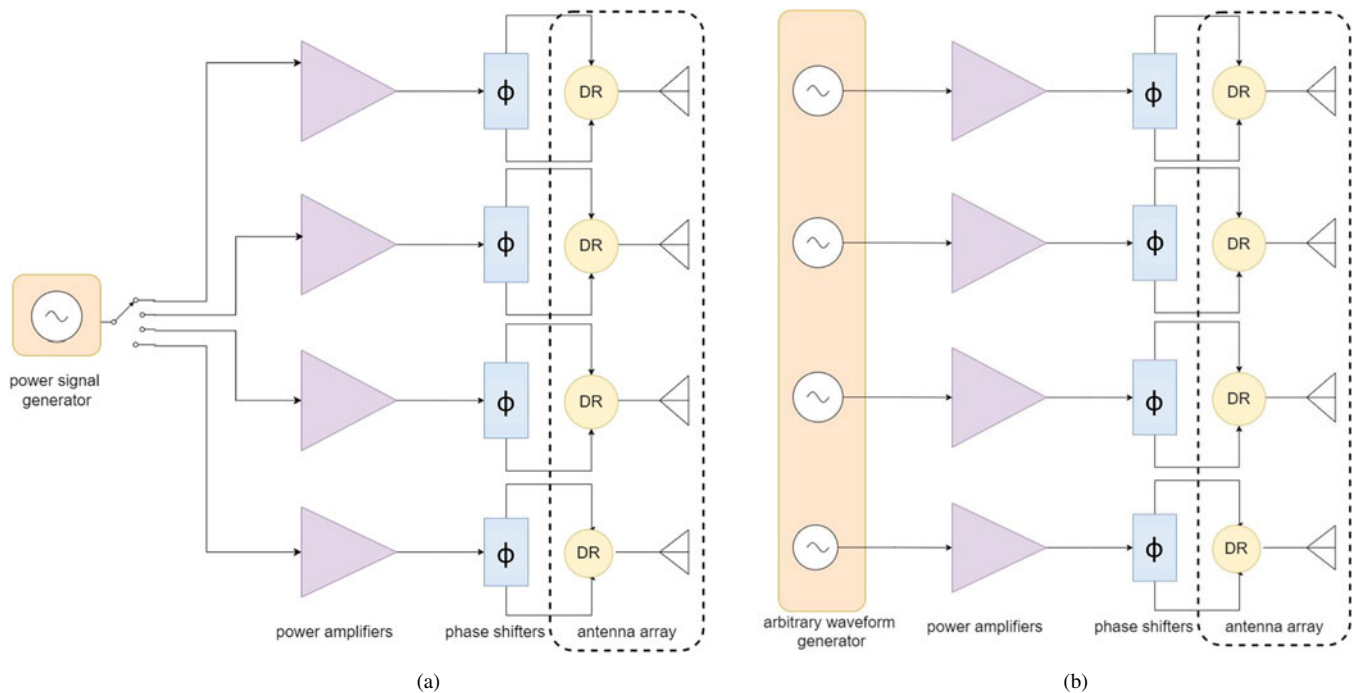


**Figure 12.** Transmit chains for multiple DRs. (a) Measurement setup II. (b) Measurement setup III.

and 30.5 GHz, respectively. In this frequency range, DR3 exhibits the highest peak gain of 11.56 at 30 GHz, while DR4 exhibits the lowest peak gain of 10.78 at 30.5 GHz.

### Simultaneous DR excitation

In measurement setup III (Figure 12(b)), a four-channel AWG was used to excite the four DRs of the RCA. Subsequently, each of the

four synchronized outputs of the AWG feeds a PA whose output, in turn, feeds each of the four phase shifters. The resulting eight signals from the output ports of the phase shifters feed the 8-port RCA by simultaneously exciting all four DRs.

The experimental setup for the multichannel transmit chain is shown in Figure 12(b). The transmit power from each of the four output ports of the AWG was set to be four times less ( $-6$  dBm) compared to measurement setups I and II. This

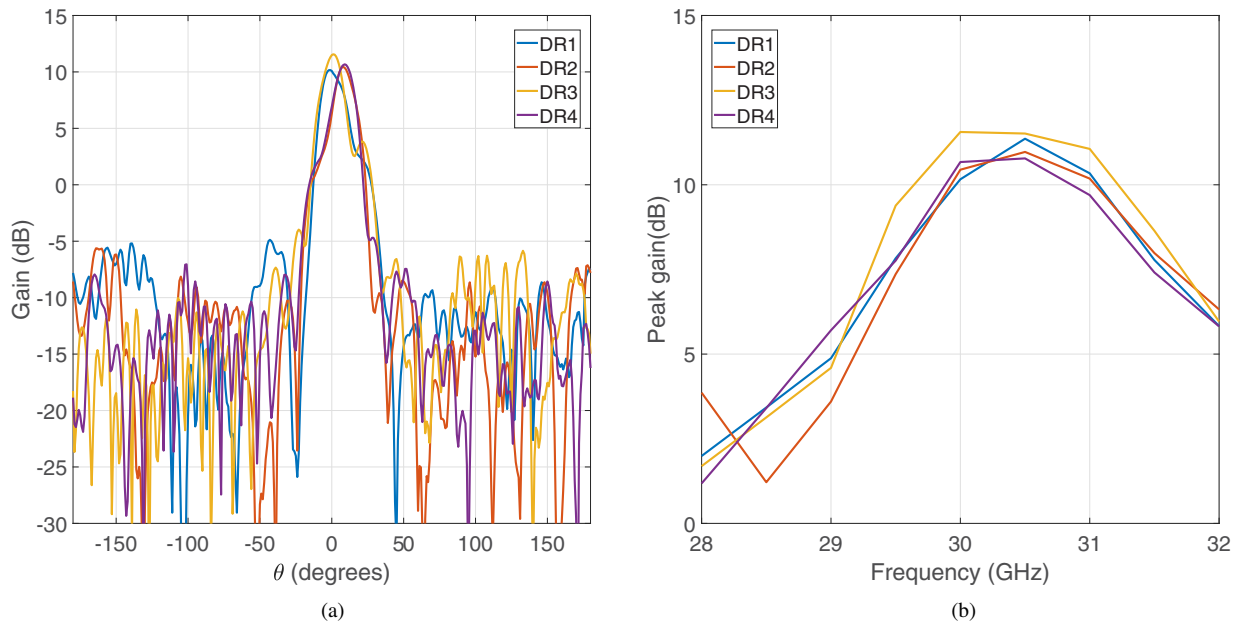


**Figure 13.** Measured radiation performance of the RCA with individual DR excitation using measurement setup II. (a) Elevation plane radiation pattern cut at 30 GHz. (b) Peak gain vs frequency.

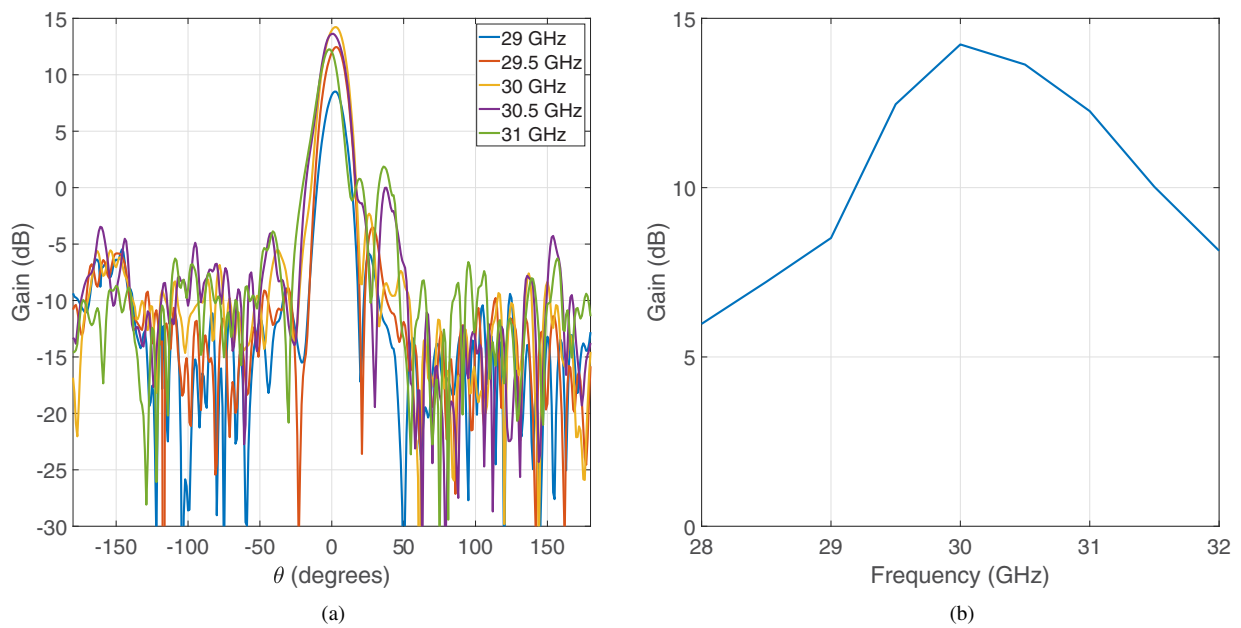


**Figure 14.** Radiation performance of the RCA with simultaneous DR excitation using measurement setup III. (a) Elevation plane radiation pattern cuts for 30–31 GHz. (b) Gain vs frequency.

power level corresponds to a peak-to-peak voltage of 0.31698 dB. Similar to measurement setups I and II, an SGH antenna was used as a receiver. The measured elevation plane radiation pattern cuts for frequencies 29–31 GHz are shown in Figure 14(a). The highest peak gain of about 11.37 dB is observed with an offset of 3° at 30 GHz. The maximum gain shows the least value of about 5.91 dB at 29 GHz with an offset of 2°. The side lobes at 30 GHz are about 16 dB below the peak value. The highest sidelobes are observed at 30.5 GHz and 31 GHz. A 3 dB beam width of about 17° is observed at 30 GHz in Figure 14(a).

Figure 15 shows the equivalent polar plot for the measured gain of the multi-feed RCA for frequencies from 29 GHz to 31 GHz.

Figure 14(b) shows the measured gain versus frequency plot for the multi-feed RCA for the frequency range 28–32 GHz at boresight as measured in an anechoic chamber. A maximum gain of about 11.2 dB is observed with a 3 dB bandwidth of about 2.0 GHz. The highest measured gain is observed to be at 30 GHz, which is consistent with the observations from Figure 14(a).

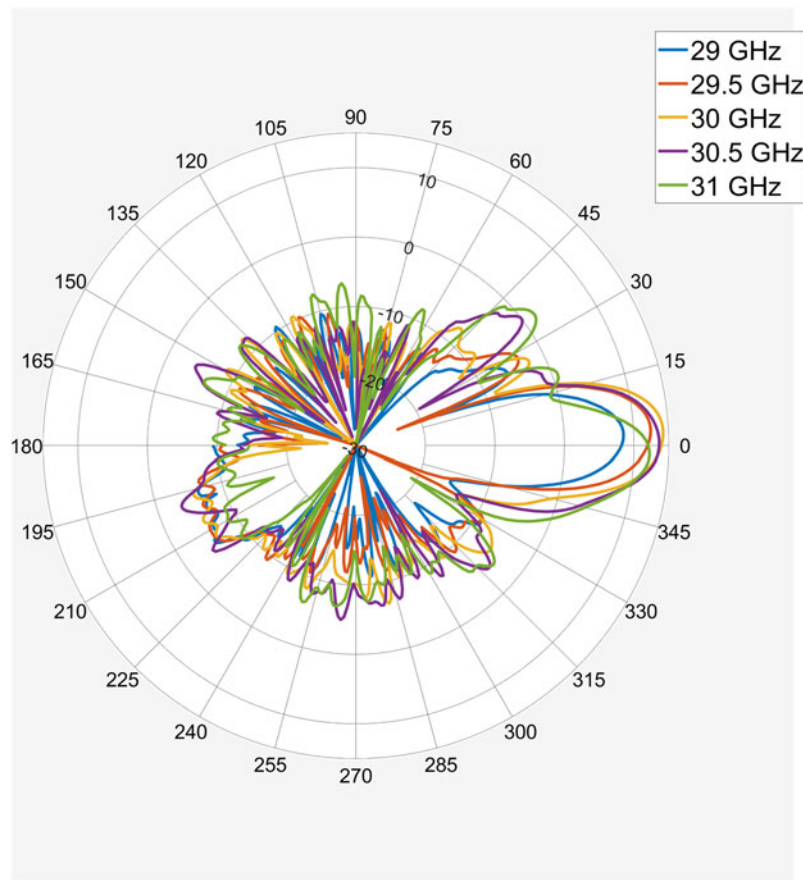


**Figure 15.** Measured polar plots for the gain of the RCA at five different frequencies.

**Table 2.** Summary of key results from simulation, measurement setups I and II

	Simulation		Measurement setup I		Measurement setup II	
	Offset (degrees)	Peak gain (dB)	Offset (degrees)	Peak gain (dB)	Offset (degrees)	Peak gain (dB)
DR1	-1.5	14.69	-3.0	9.74	-1.5	10.16
DR2	1.0	15.02	9.0	9.49	8.0	10.45
DR3	-1.0	15.03	0.0	10.58	1.0	11.56
DR4	1.5	14.69	10.0	10.09	9.0	10.67
Figure	Figure 4(a)		Figure 11(a)		Figure 13(a)	

## Analysis and discussion of results

### Individual DR excitation

We compare the simulated results for individual DR excitation with the experimental results obtained using measurement setup I and measurement setup II. First, we compare the elevation plane radiation pattern cuts at 30 GHz. We then compare the simulated gain against frequency plots for individual DRs with the measured results. These key results for radiation pattern and gain against frequency plots are summarized in Table 2, later in this article.

### Elevation plane radiation pattern cuts

The simulated elevation plane radiation pattern cuts at 30 GHz are shown in Figure 4(a) while the equivalent measured results from measurement setup I are shown in Figure 11(a). The measured results for measurement setup II are shown in Figure 13(a).

The peak gains for each DR in both the simulated and measured results at 30 GHz have offsets on similar sides with respect to 0° (i.e., DR1 and DR3 are on the same side, while DR2 and DR4 have offsets on the opposite side of 0°). While the observed offsets for these peaks exhibit symmetry in the simulated results (see Figure 4(a)), the symmetry in measured results degrades with measurement setup I exhibiting more symmetry compared to measurement setup II. The extra degradation in symmetry observed in the results for measurement setup II is because in measurement setup I, the same signal transmit path is the same for each DR, whereas the signal paths are different in measurement setup II.

In the simulated results (see Figure 4(a)), the peak gains for DR2 and DR3 are slightly higher by about 0.33 dB compared to DR1 and DR4. The offsets for DR1 and DR4 are at -1.5° and 1.5° respectively, while the offsets for DR2 and DR3 are at 1.0° and -1.0° respectively.

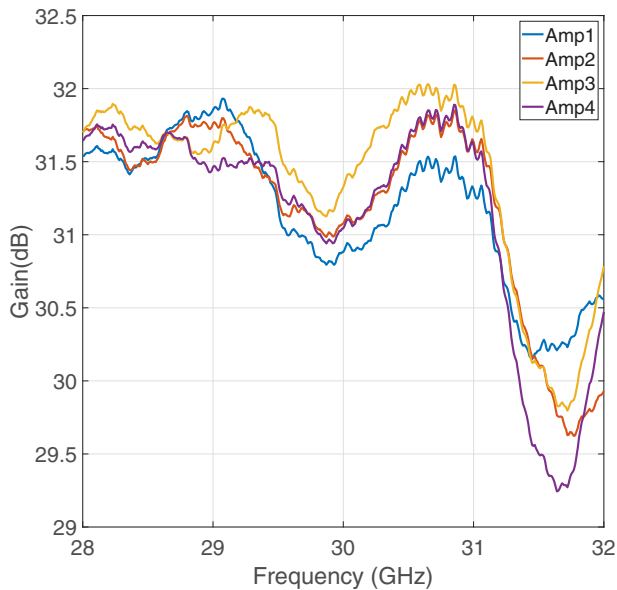


Figure 16. Amplifier gain vs frequency.

In the results from measurement setup I (Figure 11(a)), the peak gains for DR3 and DR4 are slightly higher by up to 1 dB compared to DR1 and DR2. The offsets for DR1 and DR2 are on opposite sides with respect to those of DR3 and DR4 and closely resemble the simulation results. The offsets, however, are much bigger, and the axis of symmetry for the main beams of all the DRs is no longer at 0°.

In the results from measurement setup II (Figure 13(a)), the peak gain for DR3 is highest, by about 1 dB compared to DR1, DR2, and DR4, which have comparable peaks. The offsets for DR1 and DR2 are also on opposite sides of the axis of symmetry with respect to the offsets for DR3 and DR4. This observation is similar to the results from simulation and measurement setup I with relatively minor variations. This deviation of results in measurement setup I from those obtained using measurement setup II can be attributed to the variations across the four transmit paths in measurement setup II. It should be noted that the characteristics for DR1 are the most consistent across measurement setups I and II since this transmit path for DR1 does not change across the two measurement setups.

#### Gain vs frequency plots

With individual DR excitation, we compare the simulated gain against frequency results in Figure 5(a), with the experimental results using measurement setup I in Figure 11(b) and measurement setup II in Figure 13(b). Across Figures 5(a), 11(b), and 13(b), gain against frequency plots exhibit similar trends. Results from measurement setup II (see Figure 13(b)) show a distinct variation in gain for DR3 being visibly higher than in measurement setup I (Figure 11(b)). This is attributed to the characteristic of the amplifier on the transmit path for DR3 (see Figure 16). The gain for amplifier 3 is consistently higher (by about 0.25 dB) compared to the rest of the amplifiers, over the frequency range 29.2–31.1 GHz.

#### Simultaneous DR excitation

We compare the simulated results for simultaneous DR excitation with the experimental results using measurement setup III.

Table 3. Summary of key RCA results from simulation, measurement setup III

	Simulation	Measurement setup III
Peak gain (dB)	19.36	14.23
3 dB gain bandwidth (GHz)	1.90	2.00
3 dB beamwidth (degrees)	15.00	17.00
S11 (dB)	All ports below -8 dB	All ports below -8 dB except port 1*
	(28.8–32.5 GHz)	(27.8–30.7 GHz)
Figure	Figures 3, 5(b), and 6(b)	Figures 7, 14(a), and 14(b)

\*The reflection at port 1 is below -6 dB for the frequency range 27.6–28.5 GHz and is below -8 dB for 28.5–30.2 GHz.

First, we compare the simulated elevation plane radiation pattern cuts. We then compare the simulated gain against frequency plots with the measured results. The key radiation pattern and gain against frequency results for simultaneous excitation are summarized in Table 3.

#### Elevation plane radiation pattern cuts

The measured radiation patterns for multiple frequencies from 29 GHz to 31 GHz are shown in Figure 14(a) while the simulated elevation plane radiation patterns are shown in Figures 4(a) and 6(b). Measured polar plots of gain at five different frequencies are shown in Figure 15. In both simulated and measured results, we observe that the highest gain occurs at the intended design frequency of 30 GHz, while the lowest gain occurs at 29 GHz.

#### Gain vs frequency plots

The plots for the measured gain against frequency are shown in Figure 14(b), while the simulated results are presented in Figure 5(b). Across Figures 5(b) and 14(b), the plots exhibit similar trends.

#### Conclusion

A design for a high-gain, 8-input RCA is presented in this article. The simulation results provide extensive information about the antenna and its radiation performance. Although the measured results follow a similar trend to the predicted outcomes from the full-wave EM simulations, there are some variations. The discrepancy between the simulated and measured results can be attributed to various factors, including the complex measurement approach required for multi-input excitation within the antenna, fabrication, and assembly errors, improper calibration of the antenna chamber, and issues with associated components such as connectors, adapters, and RF coaxial cables. Additionally, we believe that the antenna mount may be affecting overall antenna performance by blocking signal leakage from the edges, which is necessary to weaken the coupling between the feeding elements, thereby impacting the input impedance of the feed. A high simulated total efficiency over 81.6% is maintained across a wide frequency range of 3.8 GHz.

The antenna design is simple, cheap, and intuitive. The feeding mechanism is efficient compared to a corporate feed distribution network, which can often be lossy. The measured prototype shows

excellent matching for all input ports. A maximum simulated realized gain of 19.44 dB is achieved, making the antenna applicable to mm-wave communication systems. Recently, a compact, double-sided, 16-input port DR-based antenna was presented in [14]. This antenna is built for wireless access point applications at sub-6 GHz frequency. Despite multiple input ports and good isolation between the feeding elements, this antenna was not analyzed for its power-combining capability. This emphasizes the novelty of our approach. Additionally, the proposed RCAs can be used to create arrays with a larger aperture.

First, for the proposed RCA design, we performed measurements with all eight excitations coming directly from the AWG. This eliminates the need for phase shifters, which introduce further imperfections to the signal that the RCA receives. Furthermore, the PRS design is strategically arranged in the form of an array to achieve similar gain and directivity enhancement. We plan to implement such a topology in our future work and to design a high-power beam-steering antenna system. The beam-steering can be achieved either actively by introducing a phase shift between the feeding elements or passively by using a pair of metasurfaces as add-on devices and implementing the concept of the Risley prism to direct the beam of the antenna in a 3D conical volume.

**Acknowledgements.** The authors would like to express their gratitude to Mr. James Trasy for his help in automating and conducting measurements and to Mr. David Burdon for fabricating the antenna mount.

**Competing interests.** The author(s) declare none.

## References

1. Ali Sehrai D, Khan J, Abdullah M, Asif M, Alibakhshikenari M, Virdee B, Ali Shah W, Khan S, Ibrar M and Jan S (2023) Design of high gain base station antenna array for mm-wave cellular communication systems. *Scientific Reports* 13(1), 4907.
2. Mane PR, Kumar P and Tanweer Ali MGNA (2023) Planar MIMO antenna for mmWave applications: Evolution, present status & future scope. *Heliyon* 9(2), e13362.
3. Herranz-Herruzo JI, Ferrando-Rocher M, Valero-Nogueira A, and Bernardo-Clemente B (2023) Wideband circularly-polarized mm-wave array antenna using H-shaped low-axial-ratio apertures. *IEEE Transactions on Antennas and Propagation* 71(5), 4564–4569.
4. Gonzalez Marin J, Baba AA, Hesselbarth J, Hashmi RM and Esselle KP (2020) Millimeter-wave low-loss multifed superstrate-based antenna. *IEEE Transactions on Antennas and Propagation* 68(5), 3387–3396.
5. Chittimoju G and Devi Yalavarthi U (2021) A comprehensive review on millimeter waves applications and antennas. In *Journal of Physics: Conference Series*. IOP Publishing, Vol. 1804, p. 012205.
6. Gonzalez Marin J, Baba AA, Lopez Cuenca D, Hesselbarth J, Hashmi RM and Esselle KP (2019) High-gain low-profile chip-fed resonant cavity antennas for millimeter-wave bands. *IEEE Antennas and Wireless Propagation Letters* 18(11), 2394–2398.
7. Singh K, Attygalle M, Thalakituna D and Esselle K (2024) Multi-feed resonant cavity antenna with in-antenna power combination for mm-wave communication. In *2024 18th European Conference on Antennas and Propagation (EuCAP)*. IEEE, pp. 1–5.
8. López Cuenca D (2018) On-chip Spherical Dielectric Resonator-based Millimeter-wave Components. PhD thesis, Universität Stuttgart
9. Alberto González Marin J (2020) Functional Dielectric-based Multi-feed Antennas. PhD thesis, Universität Stuttgart
10. DigiKey. <https://www.digikey.com.au/en/models/6050848> (Online; accessed 19 March 2025).
11. Feresidis AP, Goussetis G, Wang S and Vardaxoglou JC (2005) Artificial magnetic conductor surfaces and their application to low-profile high-gain planar antennas. *IEEE Transactions on Antennas and Propagation* 53(1), 209–215.
12. Baba AA, Hashmi RM, Esselle KP, Gonzalez Marin J and Hesselbarth J (2019) Broadband partially reflecting superstrate-based antenna for 60 GHz applications. *IEEE Transactions on Antennas and Propagation* 67(7), 4854–4859.
13. Singh K, Mulinde R, Attygalle M, Thalakituna DN and Esselle KP (2024) Experimental validation of multi-feed resonant cavity antenna for mm-wave communication. In *18th International Conference on Signal Processing and Communication Systems (ICSPCS)*. IEEE, pp. 1–6.
14. Das G, Kumar Sahu N and Kumar Gangwar R (2020) Dielectric resonator based multiport antenna system with multi-diversity and built-in decoupling mechanism. *AEU-International Journal of Electronics and Communications* 119, 153193.



**Khushboo Singh** (Member IEEE) is a Research Fellow at the University of Technology Sydney. She earned a doctoral degree in electronics engineering from Macquarie University, Australia, in 2021. She was awarded a silver medal and a certificate of merit for her undergraduate degree. She also received a prestigious merit-based LNMIIT scholarship during her master's studies. She was a recipient of the highly competitive Australian government-funded iRTP scholarship for her

Ph.D. Two main themes that best summarize her recent post-doctoral research endeavors are high-gain, metasurface-based beam-steering antennas and mm-wave high-power planar array antennas. In addition, she is developing reconfigurable intelligent surfaces (RIS) and metasurfaces. She is actively involved in cutting-edge research and collaborates on critical projects with the Defence Science and Technology Group and the NSW government. <https://profiles.uts.edu.au/Khushboo.Singh>.



**Dushmantha N. Thalakituna** (Senior Member, IEEE) received the B.Sc. degree in electronics and telecommunication from the University of Moratuwa, Sri Lanka, in 2008, and the Ph.D. degree in electronic engineering from Macquarie University, Sydney, NSW, Australia, in 2012. He is currently a Senior Lecturer with the School of Electrical and Data Engineering, University of Technology Sydney, Sydney. From 2013 to 2019, he worked in multiple radio frequency and systems

engineering roles, designing antennas and monolithic microwave integrated circuits (MMICs) and radio frequency (RF) systems for both commercial and defense industries. His current research interests include MMICs, SATCOM antennas, base station antennas, reconfigurable microwave and millimeter-wave circuits, metasurfaces, and periodic structures. Dr. Thalakituna is a member of IEEE Antennas and Propagation Society and IEEE Microwave Theory and Techniques Society. <https://profiles.uts.edu.au/Dushmantha.Thalakituna>.



**Karu Esselle** received the B.Sc. degree (Hons.) in electronic and telecommunication engineering from the University of Moratuwa, Moratuwa, Sri Lanka, in 1983, and the M.A.Sc. and Ph.D. degrees (with near-perfect GPA) in electrical engineering from the University of Ottawa, Ottawa, ON, Canada, in 1987 and 1990, respectively. He is a Distinguished Professor in Electromagnetic & Antenna Engineering at the University of Technology Sydney and is a world leader in

Telecommunications, Defence and Space technologies. In 2021, his publications received over 1400 citations. His H-index is 53 and i-10 is 212. In addition to the IEEE Kanda Award mentioned above, several of his papers have been among the most cited or most downloaded. His research activities are posted on the web at <http://web.science.mq.edu.au/esselle/> and <https://www.uts.edu.au/staff/karu.esselle>.